Impact of Porosity and Velocity on the Dissolution Behaviors of Calcium Aluminate Inclusions in CaO-SiO_2-Al_2O_3 Steelmaking Slag
In Situ Observations and Model Advancements

Wang, Guang; Nabeel, Muhammad; Dogan, Neslihan; Abid, Moin; Mu, Wangzhong; Phillion, A. B.

DOI
10.1007/s11663-025-03556-1

Publication date
2025

Document Version
Final published version

Published in
Metallurgical and Materials Transactions B: Process Metallurgy and Materials Processing Science

Citation (APA)
Wang, G., Nabeel, M., Dogan, N., Abid, M., Mu, W., & Phillion, A. B. (2025). Impact of Porosity and Velocity on the Dissolution Behaviors of Calcium Aluminate Inclusions in CaO-SiO_2-Al_2O_3 Steelmaking Slag: In Situ Observations and Model Advancements. *Metallurgical and Materials Transactions B: Process Metallurgy and Materials Processing Science*, *56*(4), 3415-3427. https://doi.org/10.1007/s11663-025-03556-1

Impact of Porosity and Velocity on the Dissolution Behaviors of Calcium Aluminate Inclusions in CaO-SiO_2-Al_2O_3 Steelmaking Slag: *In Situ* Observations and Model Advancements

GUANG WANG, MUHAMMAD NABEEL, NESLIHAN DOGAN, MOIN ABID,
WANGZHONG MU, and A.B. PHILLION

The dissolution process of $CaO{\cdot}2Al_2O_3$ (CA2) particles in CaO-SiO_2-Al_2O_3 steelmaking slags was *in situ* investigated at 1550 °C. To better understand the role of particle porosity in dissolution kinetics, the particles with two different porosity levels, *i.e.,* 0.08 and 0.20 were used in this study. The porosity (φ) and surface area of CA2 particles were characterized through X-ray Computed Tomographic Imaging (XCT), and the surface area ratio ($f(\varphi)$) between the porous and full dense particles was expressed as $f(\varphi) = 0.9398e^{5.9498\varphi}$. The obtained results indicated that an increase in the porosity from 0.08 to 0.20 led to an increase in the average dissolution rate from 0.35 to 0.59 μm/s. Moreover, the motion of CA2 particles during the dissolution process was observed, suggesting its importance to include in the modeling approach. A novel mathematical model was developed to predict the dissolution time of inclusion particles by incorporating both the motion and porosity of particles. This model was validated against the existing literature data and aligned well with the current experimental findings. The model predictions demonstrated that the dissolution time of CA2 particles was decreased with an increase in the velocity and porosity of particles and concentration difference of dissolving species between particle–slag interface and molten slag (ΔC), and a decrease in slag viscosity.

https://doi.org/10.1007/s11663-025-03556-1

I. INTRODUCTION

PARTICLE motion and dissolution behavior are widely investigated in both engineering and scientific applications. One of their vital applications in metallurgy is the control of steel cleanliness, where the dissolution process of non-metallic inclusions, referred to as "NMIs" herein, plays a critical role.[1] Once the NMIs enter the slag phase, they are expected to be dissolved in the molten slag as rapidly as possible. Any NMIs that remain as the undissolved particle may re-entrain into the molten steel, posing a significant industrial risk. They may agglomerate or coalesce, leading to clogging of the submerged entry nozzle, thus, compromising product quality and production efficiency.

The dissolution mechanisms and kinetics of NMIs in slags have been well studied through experiments[2–4] and simulations[5–8] to support optimization of their removal efficiency from liquid steel during secondary refining of steelmaking. In the past two decades, *in situ* observation via High-Temperature Confocal Laser Scanning Microscopy (HT-CLSM),[9–14] and Single Hot Thermocouple Technique (SHTT),[15,16] are the most common experimental methods used to investigate the dissolution process of NMIs. These techniques allow for real-time *in situ* observation of the dissolution behavior of micron-size particles in molten slags. The main advantages of HT-CLSM to STHH are (1) image quality, (2) experimental temperature maintenance, and (3) reduced particle/slag mass ratio.[17] This third point is particularly important since high particle/slag mass

---

GUANG WANG, MUHAMMAD NABEEL, MOIN ABID, and A.B. PHILLION are with the Department of Materials Science and Engineering, McMaster University, Hamilton, ON L8S4L7, Canada. Contact e-mail: wangg84@mcmaster.ca. NESLIHAN DOGAN is with the Department of Materials Science and Engineering, McMaster University and also with the Department of Materials Science and Engineering, Delft University of Technology, Mekelweg 2628CD, Delft, The Netherlands. Contact e-mail: n.d.dogan@tudelft.nl. WANGZHONG MU is with the Department of Materials Science and Engineering, KTH Royal Institute of Technology, Brinellvägen 23 10044, Stockholm, Sweden and also with the Engineering Materials, Department of Engineering Science and Mathematics, Luleå University of Technology, Laboratorievägen 97187, Luleå Sweden.

Manuscript submitted January 21, 2025; accepted April 7, 2025.

ratio (>1.0 wt pct) could cause the change of slag composition and properties during the particle dissolution process.[10,18] The STHH typically employs a particle/slag mass ratio at around 5 wt pct magnification, significant exceeding 1 wt pct.[16,19,20] In contrast, the particle/slag ratio used in HT-CLSM is less than 0.5 wt pct.[11,21]

The NMIs' size evolution with time, recorded by CCD camera (HT-CLSM), generates a dissolution profile that can be used to validate models of dissolution mechanisms. Table I summarizes prior literature on the dissolution of NMIs in steelmaking slags via HT-CLSM. In these studies, however, it has been assumed that (1) the NMIs are nonporous particles, and (2) solute transfer related to NMI motion can be ignored. However, it is unlikely that NMIs are fully dense given the fact that, after they form within the liquid steel, they undergo growth by coalescence and agglomeration. Moreover, as listed in Table I, the motion and rotation of NMIs have been observed in many studies, but their impacts on the kinetics have not been adequately included within relevant dissolution mechanism models.

Previous investigations have primarily focused on the dissolution mechanisms and/or kinetics of Al_2O_3,[2,4,9,12,14,22–34] MgO,[12,22,24,25,35] CaO,[13,36] SiO_2,[10,21,37] ZrO_2,[25,27] $MgAl_2O_4$,[22,25,27,38] $TiO_2{\cdot}Al_2O_3$,[4,39] and $CaO{\cdot}2Al_2O_3$ (CA2)[11] in the ternary CaO-SiO_2-Al_2O_3-based slag systems at temperatures ranging from 1250 to 1600 °C, and for particle sizes that vary between 50 and 500 μm. The obtained findings indicate that the dissolution kinetics of NMIs are enhanced with increasing temperature and the concentration difference of dissolving species between the NMI–slag interface and bulk slag [*i.e.,* the driving force (ΔC)]. However, dissolution kinetics are diminished with an increasing slag viscosity.[9,21,23,28,29,35,36] It has also been reported that the dissolution rate of Al_2O_3 inclusions is increased using slags with high ratios of CaO/Al_2O_3 or CaO/SiO_2.[2,23,33]

A widely accepted approach for modeling the dissolution mechanism of NMIs in molten slag is the application of the so-called shrinking core model.[40] In this model, the limiting step for NMI dissolution is categorized as either chemical reaction (CR) control or boundary layer diffusion (BLD) control.[40] A separate approach, known as diffusion in a stagnant fluid model (DS), has also been used to interpret the dissolution mechanism of NMIs.[41] The dissolution profiles for CR, BLD, and DS, after dimensionless treatment, exhibit a unique profile shape: linear for CR, parabolic for BLD, and sigmoidal for DS. The actual dissolution mechanism of an NMI can be determined by comparing the models' prediction with the experimental dissolution curve. For instance, if the normalized experimental dissolution curve is parabolic, then the dissolution mechanism of NMI is believed to be BLD. As tabulated in Table I, prior researchers have primarily identified either BLD or DS as the main mechanisms controlling particle dissolution. Only a few studies[24,25] have reported CR as the limiting step, and even fewer[23] reported mixed control as the limiting step (*i.e.,* CR + BLD, indicating the formation of a solid product layer during dissolution). Nevertheless, it is not uncommon for different researchers to identify varying dissolution mechanisms for similar particle/slag systems. For example, Monaghan *et al.* reported that BLD was the limiting step for Al_2O_3 particles in the CaO-Al_2O_3-SiO_2 slag system, while DS was reported by Ren *et al.*[33,34] in a similar slag system with slight compositional differences.

NMIs have been observed to not only dissolve but also to move, rotate, and dissociate within the molten slag during dissolution, as schematically illustrated in Figure 1. Such phenomena could significantly impact dissolution mechanisms and kinetics by altering the fluid dynamics at the oxide-slag boundary, resulting in the shape change of the experimental dissolution curve.[23,35,42] Unfortunately, none of CR, BLD, and DS account for the motion of NMIs, which may explain the differences between the experimental and model prediction results.[28,35] Pan *et al.*[42] incorporated the velocity of NMIs via the Péclet number to consider the convective mass transfer of the dissolving component. A better fit was obtained between model predictions and experimental results. However, the velocity was calculated based on the rotation of the NMIs, which normally only occurs for a specified duration and not over the entire dissolution process. As a result, the fixed angular velocity likely does not accurately represent the true velocity over time.

Another factor beyond NMI motion that must be considered is the porosity of NMIs. Since inclusion agglomeration occurs during industrial operations, the morphology of such agglomerated inclusions has been well studied, showing that they have porosity.[43,44] For example, Yin *et al.*[45] observed that solid calcium aluminate inclusions were irregular in shape with coarse tips and pores.

The removal efficiency of NMIs from liquid steel during the refining process highly depends on their dissolution mechanisms and kinetics. Therefore, a better understanding of these processes requires investigating how the motion and porosity of NMIs affect their dissolution behaviors. Advancing conventional models to incorporate these factors will enable a more accurate determination of the dissolution mechanisms and prediction of the dissolution time of NMIs. In this study, the dissolution of $CaO{\cdot}2Al_2O_3$ (CA2) particles was examined via HT-CLSM within synthesized CaO-Al_2O_3-SiO_2 metallurgical slag. Prior to experimentation, X-ray computed tomography (XCT) was used to quantify the porosity and surface area of the investigated CA2 particles. The results were used to develop a novel model that incorporates NMI motion and porosity on dissolution kinetics.

II. METHODOLOGY

A. *Experiments*

1. *Material*

High-purity laboratory-grade powder of CaO, Al_2O_3, SiO_2, and $CaCO_3$ (Alfa Aesar) was used to produce synthetic inclusion particles and slags. To remove moisture, the CaO was roasted in a Si-Mo rod box type

Table I. Summary of Literature on the Dissolution of NMIs in Various Slag Systems Using HT-CLSM

Authors	Year	T (°C)	NMI	Slag System	Observed NMI Behavior	Identified Rate Limiting Step	$D \times 10^{-10}$ (m^2/s)
Sridhar *et al.*[9]	2000	1450–1550	Al_2O_3	CASM	rotation, dissociation	BLD	
Valdez *et al.*[22,23]	2001	1470–1550	Al_2O_3	CASM	rotation, the interface became smooth	mixed BLD + CR	
			MgO	CASM	morphology change, the interface became smooth	BLD	
			$MgAl_2O_4$	CASM	morphology change	mixed BLD + CR	
	2002	1470–1530	Al_2O_3	CAS-(M)	rotation (20–40s), product layer on particle surface in CASM slag. A smooth interface formed between CAS slag and particle	mixed CR + BLD	
Yi *et al.*[24]	2003	1450–1500	MgO	CAM	motion, rotation	CR	
			Al_2O_3	CAM		DS	
Fox *et al.*[25]	2004	1250–1500	Al_2O_3	CASMNLB	motion, rotation	CR	
			ZrO_2	CASMNLB	rotation, particle became transparent, smooth interface		
			MgO	CASMNLB	motion, rotation		
			$MgAl_2O_4$	CASMNLB	motion, rotation		
Monaghan *et al.*[26–28,38]	2004	1477–1577	Al_2O_3	CAS	motion, rotation	BLD	0.15–3.09
	2005	1477–1577	Al_2O_3	CAS	motion, rotation		
			$MgAl_2O_4$	CAS	motion and motion		
			ZrO2	CAS	gas bubbles generated around the particle		
	2005	1477–1577	Al_2O_3	CAS	motion, rotation	BLD	0.15–3.09
	2006	1504	$MgAl_2O_4$	CAS	rotation	BLD	0.67–2.20
Park *et al.*[12]	2006	1550	Al_2O_3	CAS	motion		
			MgO	CAS	motion		
Liu *et al.*[29,35]	2007	1500, 1600	MgO	CASM	rotation (38–46 second), detachment, particle became transparent, product layer	BLD	
	2007	1470–1630	Al_2O_3	CAS	motion	DS	0.24–0.97
Verhaeghe *et al.*[30,31]	2007	1600	Al_2O_3	CAS	motion, slight rotation	DS	0.27–0.42
	2008		Al_2O_3	CAS	motion	DS	0.22–0.28
Guo *et al.*[13,36]	2013	1480	CaO	CAS-(M)	rotation, motion, and product layer on the particle surface	mixed control (CR + BLD + PLD)	0.2–1.0
	2014	1450–1600	CaO	CAS-(M)	rotation, generation of gas bubble from the particle	formation of the IR layer	0.20–1.00
Feichtinger *et al.*[10]	2014	1450	SiO_2	CAS	rotation, motion	revised DS	0.38–2.40
Michelic *et al.*[32]	2016	1600	Al_2O_3	CASM	rotation, motion	DS	0.04–33.80
Miao *et al.*[11]	2018	1500–1600	$CaO \cdot 2Al_2O_3$	CAS	rotation, motion	BLD	0.06–5.8
Sharma *et al.*[4]	2018	1550	Al_2TiO_5	CAS	motion, rotation, color change from opaque to transparent	BLD	1–100
Tian *et al.*[37]	2018	1473–1573	SiO_2	CAS/CASM	interface becomes smooth	revised DS	0.25–0.55
Sharma *et al.*[39]	2020	1500	Al_2TiO_5	CAS	slight motion, rotation	BLD	18–28 (Al_2O_3), 25–38(TiO_2)

Table I. continued

Authors	Year	T (°C)	NMI	Slag System	Observed NMI Behavior	Identified Rate Limiting Step	$D \times 10^{-10}$ (m^2/s)
Ren *et al.*[21,33,34]	2021	1450–1580	Al_2O_3	CAS	dissociation for some particles	DS	0.047–1.1
	2022	1520–1570	SiO_2	CASM		DS	1.0–10.0
	2023	1500–1600	Al_2O_3	CAS		DS	2.8–4.1
Li *et al.*[2]	2024	1500–1600	Al_2O_3	CASM	rotation	BLD	16.6–95.2
Deng *et al.*[14]	2024	1450–1550	Al_2O_3	CASMT		BLD	2.18–4.18

A: Al_2O_3, B: B_2O_3, C: CaO, F: FeO, L: Li_2O, M: MgO, N: Na_2O, S: SiO_2, T: TiO_2.
BLD boundary layer diffusion, *CR* chemical reaction, *DS* diffusion in the stagnant slag, *PLD* product layer diffusion, *D* determined diffusion coefficient of dissolving species in slags.

resistance furnace (maximum temperature: 1200 °C) at 1050 °C for 12 h, while the Al_2O_3, SiO_2, and $CaCO_3$ were dried in a drying oven (maximum temperature: 400 °C) at 150 °C for 24 h before use.

To explore the effect of CA2 porosity on the dissolution process, two types of CA2 particles were prepared: porous (p-CA2) and dense (d-CA2). Porous CA2 particles, p-CA2, were prepared by sintering 100 g of $CaCO_3$ and Al_2O_3 powder in stochiometric amounts at 1600 °C for 24 h under an argon atmosphere. The details for powder mixing and sintering are available in one of our previous studies.[11] Dense CA2 particles, d-CA2, were obtained by melting approximately 5 g of the p-CA2 particles in a water-cooled copper mold using an arc melter. The slag composition used in this study, *i.e.,* 33CaO-18Al_2O_3-49SiO_2 (wt pct), was the same as a previous study.[19]

2. *Experiments*

An HT-CLSM (VL2000DX-SVF17SP, Yonekura) was used to carry out the CA2 particle dissolution experiments, providing continuous *in situ* observation. Technical details and operation procedures for the HT-CLSM facility are available elsewhere.[46,47] Each experiment was conducted as follows. First, approximately 0.15 g of slag was pre-melted in a platinum crucible (5 μm in diameter and 6 μm in height) within the HT-CLSM furnace. Second, a CA2 particle (either the p-type or the d-type) was placed on top of the pre-melted slag, and the assembly was heated to the experimental temperature according to a specified heating profile: rapid heating (1000 °C/min) to 50 °C below the test temperature, slow heating (50 °C/min) to the test temperature. The start time of dissolution, t_0, was defined as the time (at the test temperature) when the CA2 particle became fully immersed within the molten slag. The entire dissolution process of the CA2 particle was recorded using a CCD camera at a frame rate of 5 frames per second. The captured images have a resolution of 1024 × 1024 pixels, with each pixel corresponding to a size of 0.9 μm when using a ×5 objective lens and 2.3 μm when using a ×2 objective lens. Note that the mass of the CA2 particle used in each dissolution experiment was less than 0.1 pct of that of slag. As a result, the slag composition and properties were not affected by the dissolution of particle.

Data postprocessing was carried out using the ImageJ software[48] to determine the time evolution of the dissolution process. Each CA2 particle was segmented from the slag in each frame based on image contrast, and the particle diameter was measured. The measurements were repeated three times to reduce manual error, and then averaged. From this data, the evolution in equivalent radius, assuming a spherical particle, was determined.

3. *Characterization*

X-ray diffraction (XRD) (Panalytical X'pert diffraction instrument, using a copper source with a wavelength of 1.540 56 Å) was employed to identify the phases present within the synthesized CA2 particles.

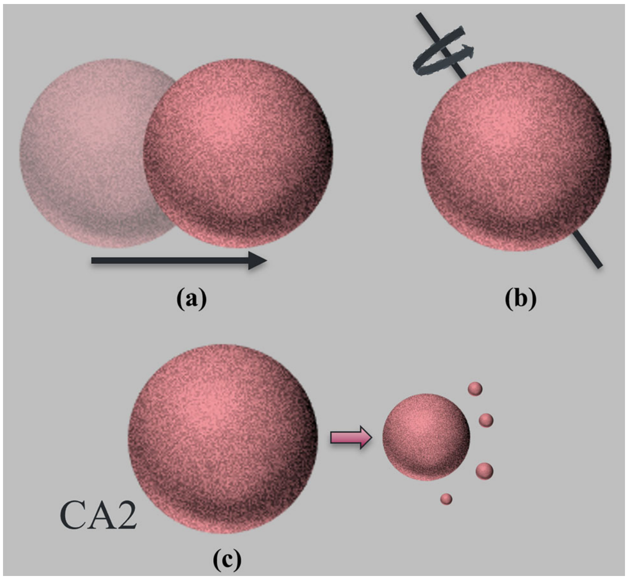

Fig. 1—Potential NMI behavior during dissolution: (*a*) motion, (*b*) rotation, and (*c*) dissociation.

X-ray computed tomography (XCT) was conducted on two p-CA2 and two d-CA2 particles using a ZEISS Xradia 630 Versa system to characterize the surface area and internal porosity of the CA2 particles. In total, two XCT scans were performed, one for each type of particle, with the same scan parameters applied for both scans. The field of view for each scan was approximately 2.6 × 2.6 mm^2, with two particles in each XCT scan. This resulted in a volumetric dataset comprising approximately 2036 × 2036 × 2036 voxels, with a voxel size of 1.3 μm. For each scan, 2401 radiographs were acquired over a 360 deg rotation with an exposure time of 5.5 seconds per radiograph. An accelerating voltage of 90 kV was used during the imaging process. The CA2 particles were sandwiched between Kapton tape layers to ensure secure positioning on the sample holder and to prevent sample fluttering during image acquisition. Postprocessing was carried out using the Dragonfly software to determine the pore number density, apparent surface area, and pore volume of CA2 particles. Due to the irregular shape of CA2 particles, the volume of the surface-connected pores could not be measured directly and only the internal pores were counted using the Dragonfly analysis software as shown in Figure 2(a). To address this challenge, the 3D XCT images of all four particles were cropped into spheres with a fixed radius $r = 150$ μm. This value was chosen since it represents the radius of the maximum sphere that can be fit within the irregularly shaped CA2 particles. The total volume of internal and surface-connected pores was measured without distinction, as cropping could convert internal pores into surface-connected ones [Figure 2(b)].

B. *Model development*

During a particle dissolution, a particle's time-dependent mass loss, $J_1(\text{m/s})$, is formulated as follows:

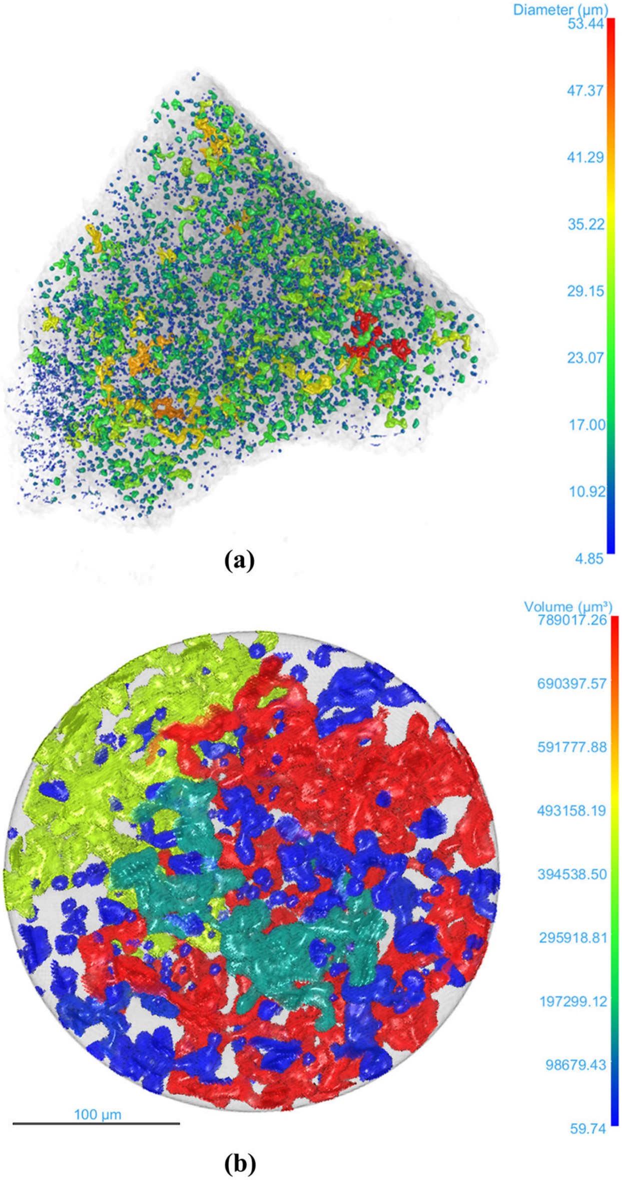

Fig. 2—X-ray computed tomography images of one d-CA2 particle prepared by arc melting (*a*) presents the original CA2 particles, and (*b*) presents corresponding cropped spheres (radius 150 μm). Color maps indicate equivalent spherical diameters (a) and pore volumes (b).

$$J_1 = -\frac{1}{S_s}\frac{dM_P}{dt}, \qquad [1]$$

where M_P is the particle mass (kg) and S_s is the surface area of the particle (m^2). By assuming that the particle is nonporous and spherical, M_P and S_s can be expressed as follows:

$$M_p = V_P\rho_P = \frac{4}{3}\pi r^3\rho_P, \qquad [2]$$

$$S_s = 4\pi r^2, \qquad [3]$$

where V_P is the particle volume (m^3), ρ_P is the particle density (kg/m^3), and r is the equivalent spherical radius (m). According to mass conservation, the loss rate of the particle J_1 must equal the mass flux, J_2 (m/s), across the boundary layer:

$$J_1 = J_2, \quad [4]$$

where J_2 can be determined from

$$J_2 = -k_m(C_{sat} - C_0), \quad [5]$$

where k_m is the apparent rate constant, C_{sat} is the saturation concentration of the dissolving species, and C_0 is the concentration of the dissolving species in the bulk slag. Coupling Eqs. from [1] through [5], the time-dependent radius gives

$$\frac{dr}{dt} = -\frac{k_m(C_{sat} - C_0)}{\rho_P}. \quad [6]$$

Chemical Reaction Control: In this approach, it is assumed that the apparent rate constant k_m is controlled by the chemical reaction rate, k_c, between the particle and molten slag, and further that k_c is a constant. Integrating both sides of Eq. [6], from r_0 to r and from 0 to τ, gives[40]

$$\frac{r}{r_0} = 1 - \frac{t}{\tau}, \quad [7]$$

$$\tau = \frac{\rho_P}{(C_{sat} - C_0)k_c}, \quad [8]$$

where r_0 is the initial equivalent radius of the particle (m). τ is the total dissolution time of the particle (seconds).

The dissolution-limiting step is considered CR if the normalized experimental dissolution curve matches the curve from Eq. [7].

Boundary Layer Diffusion Control: In this approach, it is assumed that the mass transfer rate is governed by mass transport of reactants and products to and from the slag–particle interface, and further that the thickness of the boundary layer and the concentration profile of the dissolving species can be assumed to be constant. Under conditions of "Stokes flow," the influence of convection can also be ignored. As a result, the mass transfer coefficient can be expressed as the ratio of the diffusion coefficient to the particle radius, *i.e.*, $k_m = D/r$. Integrating both sides of Eq. [6] from r_0 to r and from 0 to τ, gives[40]

$$\frac{r}{r_0} = \left(1 - \frac{t}{\tau}\right)^{1/2}, \quad [9]$$

$$\tau = \frac{\rho_p r_0^2}{2(C_{sat} - C_0)D}. \quad [10]$$

The dissolution-limiting step is determined as BLD when the normalized experimental dissolution curve aligns with the curve predicted by Eq. [9].

As discussed in the introduction, several studies have reported the motion of particles during the dissolution process, suggesting its importance to include in the modeling. Moreover, the pores within the particle, affecting the dissolution kinetics by altering the contact area between the particle and bulk slag, should also be considered in the modeling.

1. *Incorporation of particle porosity*

To incorporate particle porosity, Eqs. [2] and [3] can be rewritten as follows:

$$M_P = V_P\rho_P(1 - \varphi) = \frac{4}{3}\pi r^3 \rho_P(1 - \varphi), \quad [11]$$

$$S_s = f(\varphi)4\pi r^2, \quad [12]$$

where φ represents the particle porosity as compared to a solid sphere of equivalent diameter, and $f(\varphi)$ defines a function that represents the change in particle surface area due to surface porosity. Equation [6] then becomes

$$\frac{dr}{dt} = -\frac{k_m(C_{sat} - C_0)f(\varphi)}{\rho_P(1 - \varphi)}. \quad [13]$$

More details on the methodology for determining surface area and particle porosity are provided in Section III–A.

2. *Incorporation of particle velocity*

Convective flow resulting from particle motion enhances mass transport of the dissolving species thereby reducing the thickness of the boundary layer between slag and particle. The Péclet number, $Pe = 2rv/D$[49] where v is the particle velocity, is a dimensionless quantity used to quantify the importance of convective transport as compared to diffusive transport. In this study, it can be assumed that convection fluxes are caused by natural convection because of the density gradient in the molten slag. This is because there are no external forces within the HT-CLSM to otherwise stir the molten slag or induce particle movement. As a result, particle velocity during dissolution is given by[50,51]

For $Re < 1$,

$$v = \frac{2r^2 * (\rho_P - \rho_S) * (1 - \varphi) * g}{9\mu_s}. \quad [14]$$

For $1 < Re < 10^5$,

$$v = \sqrt{\frac{8gr(\rho_P - \rho_S) * (1 - \varphi)}{3\rho_S C_D}}, \quad [15]$$

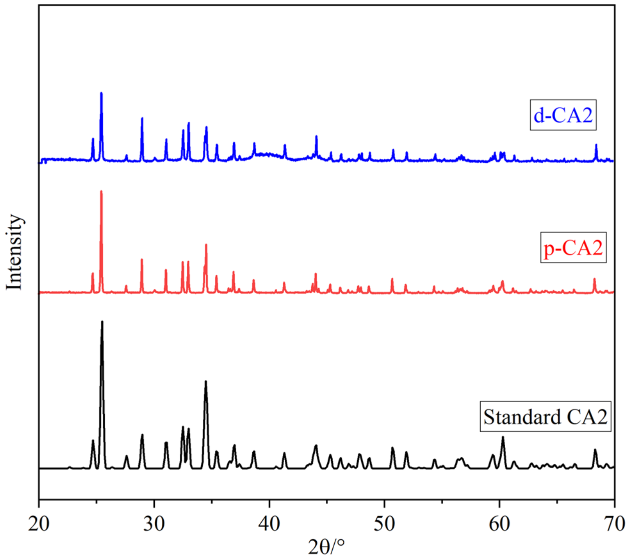

Fig. 3—XRD patterns of d-CA2 (blue line), p-CA2 (red line), and standard CA2 (black line) (Color figure online).

Table II. Summary of Physical Parameters of Cropped CA2 Particles

Particle	Pore Volume ($\times 10^6$ μm^3)	$f(\varphi)$	Fraction Porosity
p1-CA2	2.8	3.3	0.20
p2-CA2	4.1	4.1	0.29
d1-CA2	1.2	1.2	0.08
d2-CA2	1.7	2.7	0.12

$$C_D = \frac{24}{\mathrm{Re}}\left(1 + 0.15\mathrm{Re}^{0.687}\right) + \frac{0.42}{1 + 42500Re^{-1.16}}, \quad [16]$$

where $Re = \frac{2rv\rho_S}{\mu_s}$ is the Reynolds number with μ_s being the viscosity of the slag (Pa·s) and C_D is the drag coefficient. ρ_S is the density of the slag (kg/m^3) and g is the force of gravity (m/s^2).

Assuming that the mass transfer rate is governed by both the diffusion of the dissolving species as well as convection due to the particle's motion,[49]:

For $Pe \leq 10000$,

$$k_m = \frac{D\left(4 + 1.21 * Pe^{\frac{2}{3}}\right)^{\frac{1}{2}}}{2r}. \quad [17]$$

For $Pe > 10000$,

$$k_m = \frac{1.1DPe^{1/3}}{2r}. \quad [18]$$

Coupling Eqs. [13], [17], and [18], the dissolution rate is given as follows:

For $Pe \leq 10000$,

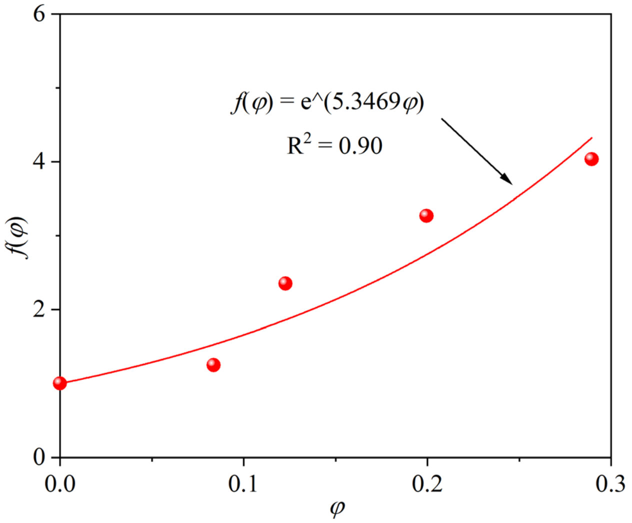

Fig. 4—XCT-determined specific surface area $f(\varphi)$ as a function of porosity, φ, along with a best-fit exponential curve through the data points.

$$\frac{dr}{dt} = -\frac{f(\varphi)(C_{sat} - C_0)D\left(4 + 1.21 * Pe^{\frac{2}{3}}\right)^{\frac{1}{2}}}{2r\rho_p(1-\varphi)}. \quad [19]$$

For $Pe > 10000$,

$$\frac{dr}{dt} = -\frac{1.1f(\varphi)(C_{sat} - C_0)DPe^{\frac{1}{3}}}{2r\rho_p(1-\varphi)}. \quad [20]$$

The above equations were numerically solved using MATLAB via the ode45 solver. This new model is named Modified Mass transfer-controlled Dissolution Model (MMDM).

III. RESULTS AND DISCUSSION

A. *Characterization of Calcium Aluminates*

Figure 3 presents the XRD patterns of d-CA2 (blue line) and p-CA2 (red line), which align well with the standard reference CA2 (black line).[52] The absence of additional phases confirms the successful synthesis of high-purity CA2 particles.

Table II provides the physical properties of the two p-CA2 and two d-CA2 particles analyzed via 3D XCT. As can be seen, the porosities of p-CA2 particles are higher than that of d-CA2 particles (0.20 and 0.29 vs. 0.08 and 010). This illustrates that the arc melting considerably reduced the porosity of the CA2 particles. In terms of surface area, the table also shows that the ratio of the effective surface area to the surface of an equivalent sphere varies from particle to particle, but the values for p-CA2 are always much greater than ones for d-CA2, further indicating the complex geometry and porosity of CA2 particles.

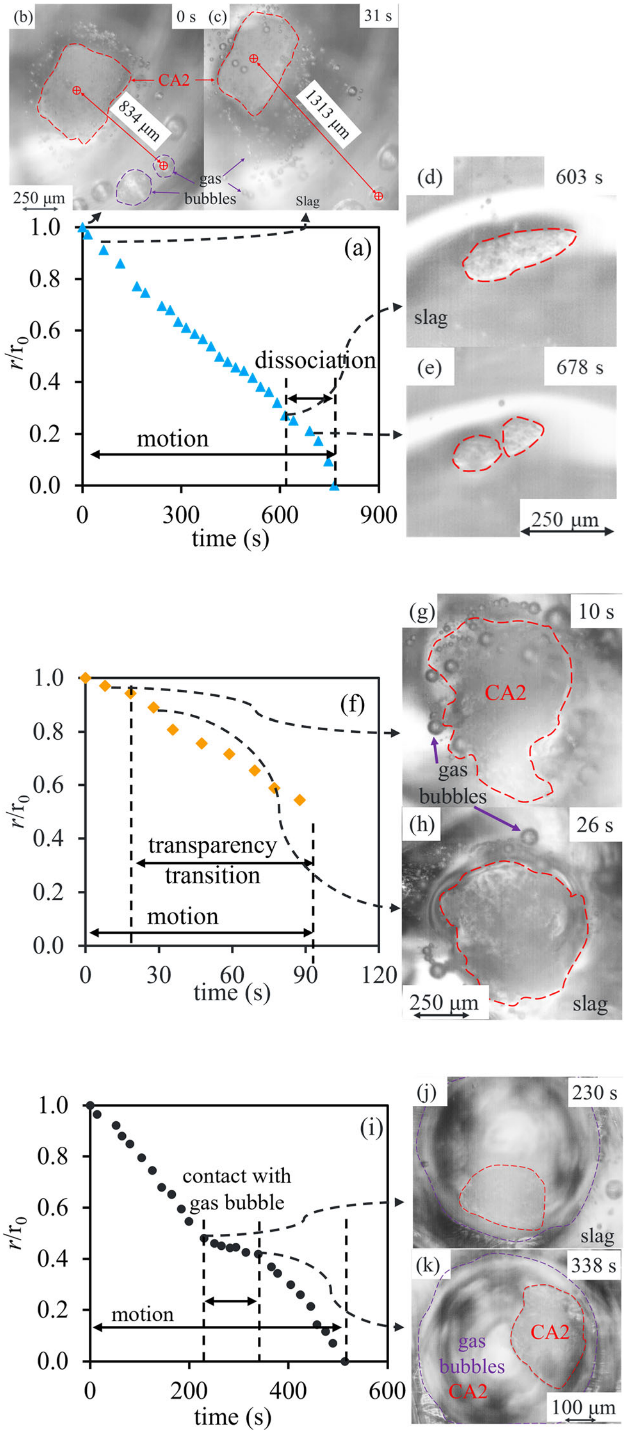

Fig. 5—Evolution of normalized radius changes of CA2 particles as a function of time in slag at 1550 °C, illustrating different CA2 particle behaviors observed during the dissolution process: (*a*) to (*e*) motion and dissociation in the slag of d1-CA2, (*f*) to (*h*) motion and transparency transition of p2-CA2, and (*i*) to (*k*) motion and interaction with a gas bubble of p-CA2.

Table III. Summary of CA2 Particle Dissolution Time and Rate at 1550 °C

particle	r_0 (µm)	r_τ (µm)	φ	τ (s)	$(r_0-r_\tau)/\tau$ (µm/s)
p2-CA2	346	0	0.20	591	0.59
d1-CA2	297	91	0.08	603	0.34
d2-CA2	105	0	0.12	295	0.35

The values of ratio, $f(\varphi)$, can be plotted as a function of porosity φ, as shown in Figure 4. It should be noted that the first data point in Figure 4 is a theoretical value, corresponding to $\varphi = 0$, where $f(\varphi) = 1$. An exponential relationship is observed between $f(\varphi)$ and φ,

$$f(\varphi) = e^{5.3469\varphi} \qquad [21]$$

Accordingly, Eqs. [19] and [20] were rewritten to incorporate this relationship,

For $Pe \leq 10000$,

$$\frac{dr}{dt} = -\frac{e^{5.3469\varphi}(C_{sat} - C_0)D\left(4 + 1.21 * Pe^{\frac{2}{3}}\right)^{\frac{1}{2}}}{2r\rho_p(1-\varphi)}. \qquad [22]$$

For $Pe > 10000$,

$$\frac{dr}{dt} = -\frac{1.1 * e^{5.3469\varphi}(C_{sat} - C_0)DPe^{\frac{1}{3}}}{2r\rho_p(1-\varphi)}. \qquad [23]$$

B. *Effect of CA2 Particle Behaviors on the Dissolution Kinetics*

During the dissolution experiments of the CA2 particles at 1550 °C in slag, various particle behaviors were observed including motion, dissociation, transparency transition, and interaction with gas bubbles. Notably, particle motion was consistently observed, whereas the other behaviors were only observed in specific experiments. Figure 5 presents a sequence of images illustrating these behaviors. The solid red and purple boundaries denote projection areas of CA2 particle and gas bubbles, respectively, with the surrounding area comprised of transparent molten slag. The corresponding dissolution curves, normalized by initial radius and segmented by behavioral sections, are also provided.

Figure 5(a) through (e) depicts the dissolution of the d1-CA2 particle, which exhibited both motion throughout the test and dissociation after 603 seconds. The particle was observed to move a considerable distance, 479 µm over the first 31 seconds, resulting in an average velocity of 15.4 µm/s. The dissociation resulted in the formation of two smaller fragments. The dissolution curve shows approximately linear behavior until dissociation. The steepened slope during the dissociation phase indicates that dissociation enhanced dissolution by increasing the contact area between the particle and molten slag. This observation underscores the importance of considering the actual surface area of a porous particle in modeling. Note that after the d1-CA2 particle dissociated into two fragments, the projection area for both fragments was measured separately via the ImageJ software.[48] The total projection area, including both fragments, was then used to determine the equivalent radius of the dissociated d1-CA2 particle.

Figure 5 (f) through (h) shows the dissolution of the p2-CA2 particle, which dissolved rather quickly and dissociated after 90 seconds. The main feature to highlight with this particle is the transition in transparency, changing from opaque to semi-transparent, from 20 to 90 seconds. Changes in inclusion transparency were also reported by Fox *et al.*[25] for an Al_2O_3 particle, Liu *et al.*[35] for a MgO particle, and Sharma *et al.*[4] for an Al_2TiO_5 particle. After 90 seconds, the semi-transparent particle dissociated into numerous smaller fragments, which subsequently dissolved rapidly. Data collected after 90 seconds was excluded as measuring the projection area of these fragments became impractical. Moreover, the p2-CA2 particle exhibited movement throughout the dissolution process.[4,25,35]

Another phenomenon observed during the dissolution process was the interaction of the particle with a gas bubble, as illustrated in Figure 5(i) through (k). This observation is for the dissolution of a p-CA2 of which porosity and surface area were not determined using XCT. The particle interacted with a gas bubble for ~118 seconds, between 230 and 338 seconds. Initially, the particle dissolved relatively quickly, but dissolution was effectively paused during the period that the particle interacted with the gas bubble. After exiting the gas bubble, the dissolution rate returned to its initial value. As a result, it is clear that the gas bubble obstructed the interaction between the p-CA2 and molten slag, thereby hindering the mass transport of dissolved species from the p-CA2–slag interface to bulk slag. Note that the radius of the particle within gas bubble was measured through projection area.

C. *Effect of CA2 Particle Porosity on the Dissolution Kinetics*

The relationship between porosity and dissolution kinetics at 1550 °C in slag can be examined by looking at the total dissolution time of three of the four CA2 particles characterized via XCT. However, dissociation occurred very early-on during the experiment for p2-CA2, and so it was excluded. Table III summarizes the dissolution time and rate of CA2 particles with different porosities. For p1-CA2 (φ of 0.20, $r_0 = 346$ μm), τ was around 591 seconds. For d1-CA2 (φ of 0.08, $r_0 = 297$ μm), τ was around 603 seconds. However, that particle only partially dissolved, to 91 μm, prior to dissociation. Finally, for d2-CA2 (φ of 0.12, $r_0 = 105$ μm), τ was around 295 seconds. This data can be used to determine a total dissolution rate, which is seen to increase from approximately 0.34 to 0.59 μm/s as the porosity increased from 0.08 to 0.20, indicating that higher porosity enhances the dissolution rate. This is attributed to the larger surface area associated with higher porosity, which increases the reaction area between particle and molten slag.

IV. VALIDATION AND APPLICATION OF MMDM

A. *MMDM Validation*

Experimental data from the literature[29] were employed to validate the MMDM and compare its performance with other conventional models. The dissolution of a spherical Al_2O_3 particle into 29.7CaO-24.1Al_2O_3-46.2SiO_2 (wt pct) slag observed using CLSM at 1550 °C, as reported by Liu *et al.*[29], was selected for validation. They employed the DS model to determine the dissolution mechanism, which assumes the NMI–slag interface is invariant. This means that the diffusion field would have stayed once the NMI–slag interface had been fixed at the beginning of the dissolution. For a spherical particle dissolution, based on Fick's first and second laws, the dissolution rate of the particle is expressed as follows[41]:

$$\frac{dr}{dt} = -\frac{C_{sat} - C_0}{C_p - C_{sat}}\frac{D}{r} - \frac{C_{sat} - C_0}{C_p - C_{sat}}\sqrt{\frac{D}{\pi t}}. \qquad [24]$$

This study was chosen due to the spherical shape of Al_2O_3 particles, aligning with a critical assumption: the particle is spherical for all four models. Moreover, Liu *et al.* reported particle motion during the dissolution process, which they identified as a primary scatter source in their experimental data. Unfortunately, the porosity of the spherical alumina particle was not specified, so a value of $\varphi = 0$ was assumed in the current model for validation. Equations [7 and 8] for CR model, Eqs. [9] through [11] for BLD model, Eq. [22] for MMDM, and Eq. [21] for DS model were solved using the parameters provided in Table IV from Liu's work.[29] The obtained normalized dissolution curves based on each model are presented in Figure 6. The spherical markers represent Liu's experimental results, while the dashed-doted, dotted, solid, and dashed lines correspond to predictions of the CR model, BLD model, MMDM, and DS model, respectively. The CR model and MMDM initially agreed with experimental data for $t/\tau < 0.20$. When t/τ is between 0.2 and 0.45, the predictions of both MMDM and DS models are close to the experimental data. Beyond 0.45, only the MMDM aligns well with experimental data. By accounting for the motion of the spherical particle in the molten slag, the MMDM offers a more accurate representation of the dissolution mechanism under experimental conditions.

To investigate the influence of particle motion on the shape of the dissolution curve, the k_m of Al_2O_3 particle in 29.7CaO-24.1Al_2O_3-46.2SiO_2 (wt pct) slag was analyzed over time using the BLD and MMDM, with parameters provided in Table IV. The CR and DS models were excluded due to their assumptions, which do not yield k_m. In contrast, the BLD and MMDM require D to determine k_m, with D values of 9.57×10^{-11} and 2.75×10^{-11} m^2/s, respectively. D is back-calculated according to the total dissolution time in both BLD and MMDM. For the same total dissolution time, different D values are obtained with different models.

Table IV. Parameters Used in the Models

r_0 (μm)	ρ_{slag} (kg/m^3)	ρ_{Al2O3} (kg/m^3)	μ (Pa s)	ΔC_{Al2O3} (kg/m^3)	D (m^2/s)	τ (s)
250	2622	3950	2.10	651	2.50E-11	1982

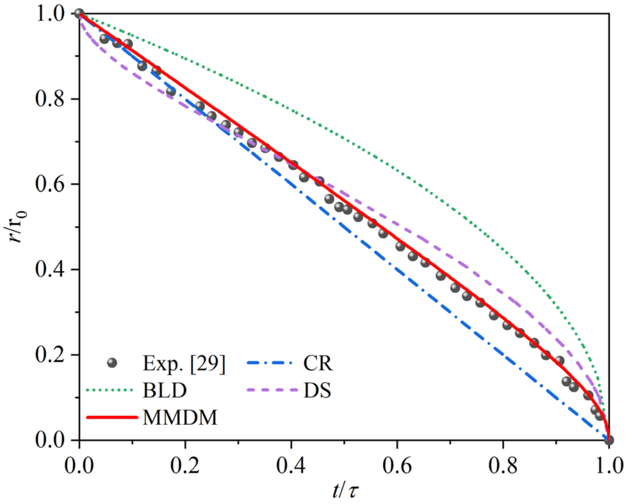

Fig. 6—Normalized dissolution curves for spherical Al_2O_3 particle in molten slag at 1550 °C compared with different dissolution rate-controlling models.

Figure 7(a) illustrates k_m as a function of t/τ. In both BLD and MMDM, k_m increases with t/τ. Initially ($t/\tau < 0.7$), the k_m in BLD is slightly lower than in MMDM. However, beyond this point, k_m in BLD surpasses MMDM, which is inconsistent with expectations. This discrepancy arises because BLD only accounts for diffusion, leading to an overestimated D. In contrast, MMDM incorporates both natural convection and diffusion, resulting in a higher k_m compared to BLD. Figure 7(b) shows the ratio of D/k_m, interpreted as the boundary layer thickness. The MMDM consistently predicts a thinner boundary layer than BLD throughout the dissolution process. Given that D remains constant for a specific particle-slag system at a fixed temperature, a thinner boundary layer corresponds to a higher k_m. Thus, particle motion effectively reduces the boundary layer thickness, enhances k_m, and leads to a steeper dissolution curve compared to the BLD model (Figure 6).

B. *MMDM Application*

1. *Determination of diffusion coefficient of CA2*

The dissolution rate-limiting step of CA2 particles was first identified by comparing normalized dissolution curves with model predictions. The best-fitted model was then applied to determine the diffusion coefficient of CA2 particle in slag at 1550 °C. The ΔC_{Al2O3} and μ are 1481 kg/m^3 and 1.36 Pa s for slag at 1550 °C, respectively, which were calculated by FactSage 8.0 with the FToxid databases.[53] The rest of the parameters required for the models' calculation can be found in Table II.

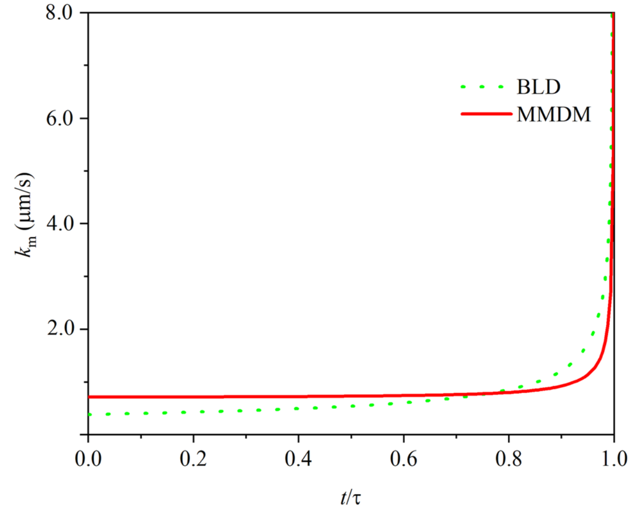

(a)

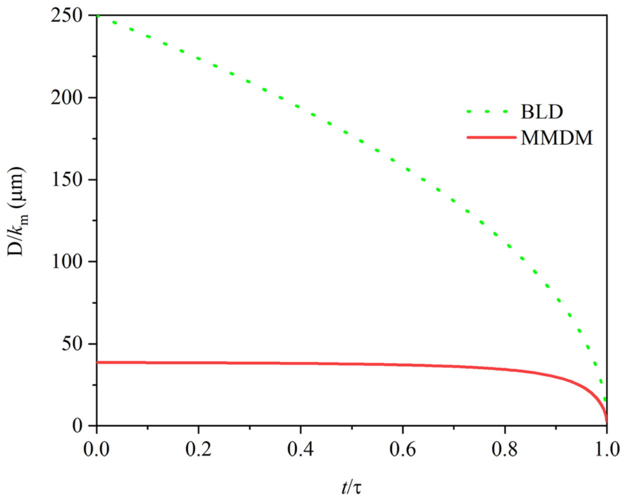

(b)

Fig. 7—(*a*) variation of k_m as a function of t/τ for BLD and MMDM. (*b*) Variation of D/k_m as a function of t/τ for BLD and MMDM.

Figure 8(a) presents normalized experimental data and predictions of four models (diamonds: experimental data, dashed-dotted line: CR, dotted line: BLD, dashed line: DS, and solid line: MMDM). As can be seen, when the t/τ is less than 0.5, both CR and MMDM aligned well with experimental data. After that, DS and MMDM agreed with the experimental data. Therefore, the MMDM has a much better fitting with experimental data by incorporating the porosity and motion of CA2 particles, indicating that mass transfer, including natural convection and diffusion, is the primary rate-limiting step for CA2 particle dissolution in the slag. The

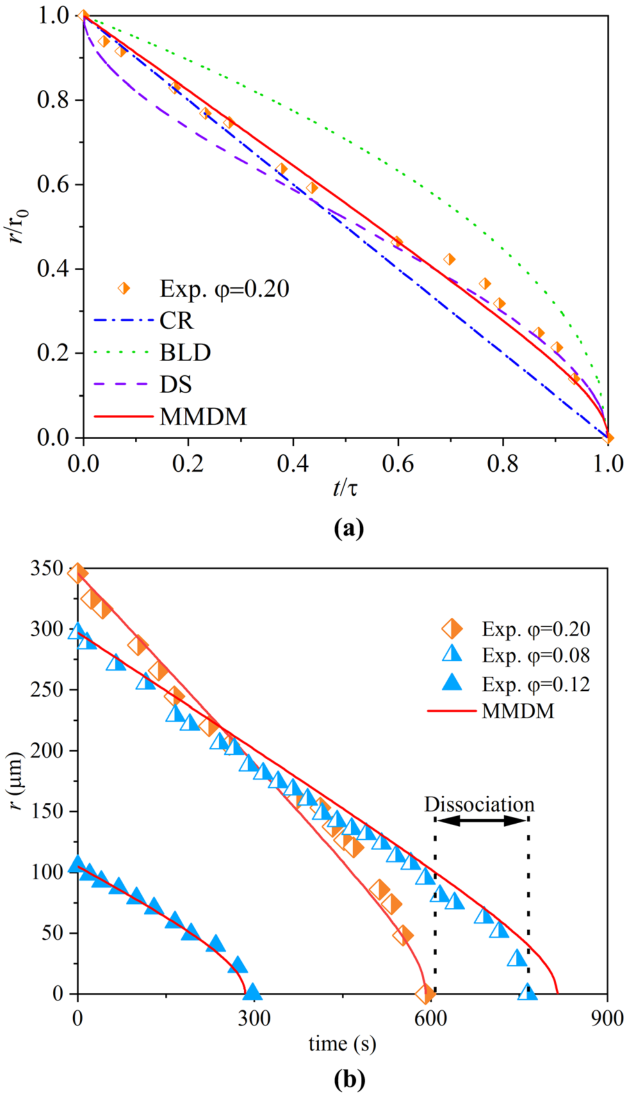

Fig. 8—(*a*) Comparison of normalized dissolution curves for p1-CA2 particles and four models, (*b*) Comparison of CA2 particle's radius change as a function of time between experiments and MMDM prediction in slag at 1550 °C.

diffusion coefficient, 1.25×10^{-11} m^2/s, of CA2 in slag at 1550 °C was determined using MMDM, which is in the range reported by the literature.[11]

The determined diffusion coefficient, 1.25×10^{-11} m^2/s, was applied to predict the dissolution time for the d1-CA2 and d2-CA2 particles using MMDM in slag at 1550 °C. As shown in Figure 8(b), the total dissolution time (including the time after dissociation) for the d1-CA2 particle with radii of 297 μm is 764, 51 seconds shorter than the MMDM prediction of 815 seconds. This discrepancy is likely due to the particle dissociation observed after 603 seconds, as discussed in Section III–B. In addition, the average velocity of CA2 particle, calculated using Eq. [14], is 14.2 μm/s, closely aligns with the experimentally measured average velocity of 15.4 μm/s, determined from the CA2 particle's displacement during the first 31 seconds of recorded dissolution images. For the d2-CA2 with a radius of 105 μm, the total dissolution time is 297 seconds, slightly exceeding the MMDM prediction of 2284 seconds by 13 seconds. Despite slight variations, the MMDM predictions

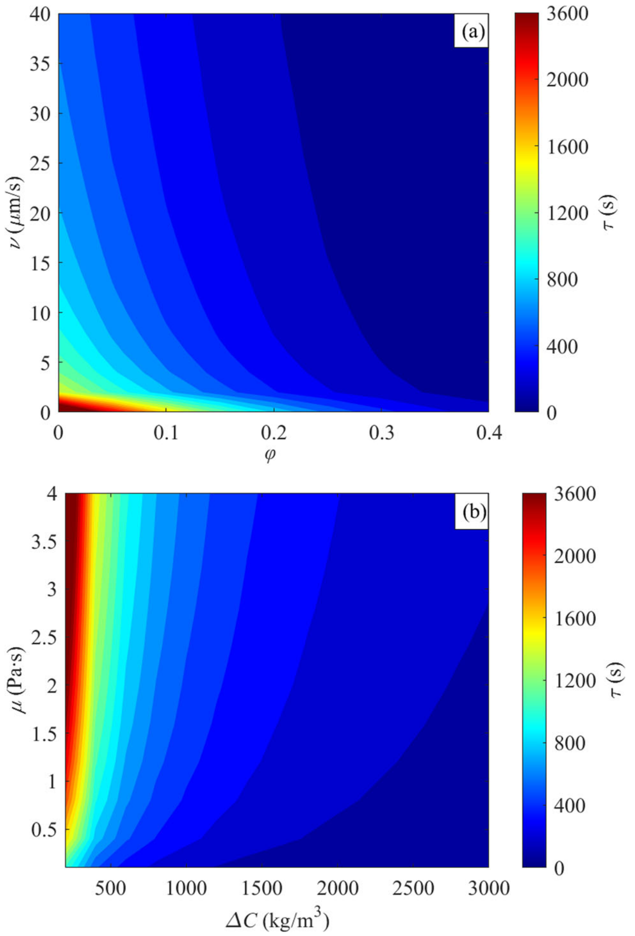

Fig. 9—Prediction of the total dissolution time of CA2 particles in CaO-Al_2O_3-SiO_2 slag at 1550 °C (*a*) variation of v and φ, (*b*) variation of μ and ΔC. (the color bar is nonuniform).

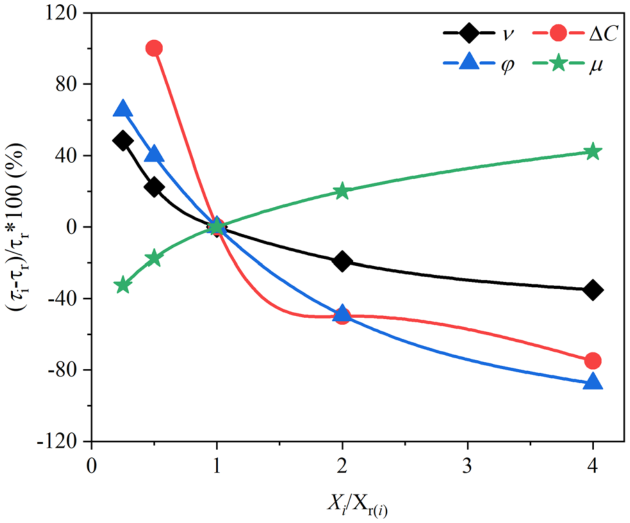

Fig. 10—Effects of parameters variation (v, ΔC, φ and μ) on the total dissolution time in percentage.

closely match the experimental dissolution times. The experimental dissolution curves for both types of CA2 particles align well with the MMDM predictions, confirming that mass transfer is the rate-limiting step for CA2 dissolution. The findings also indicate that particle porosity impacts dissolution time, underscoring its importance in predicting dissolution kinetics accurately.

2. *Prediction of CA2 dissolution time*

The MMDM model was applied to predict the total dissolution time of CA2 particles in CaO-Al_2O_3-SiO_2 slags at 1550 °C. Figure 9 shows two heatmaps, showing τ with variations in φ and v, and with variations in μ and ΔC, for $r_0 = 200\ \mu m$. Beginning with Figure 9(a), it can be seen that as v increases from 0 to 10 μm/s, τ decreases significantly, particularly for φ is less than 0.2. Beyond $v = 10\ \mu m/s$, τ decreases slightly with further increasing v to 40 μm/s. Similarly, increasing φ from 0 to 0.4 reduces τ, highlighting the role of porosity in enhancing dissolution by increasing the effective contact/surface area between molten slag and particle. The combined effects of v and φ demonstrate that higher v and φ lead to shorter dissolution times, emphasizing their importance in accurately modeling particle dissolution in slags. In Figure 9(b), it can be seen that τ was decreased when decreasing μ and increasing ΔC. Moreover, the τ is more sensitive to the low ΔC region with the same μ. For example, when $\mu = 2$ Pa s, increasing ΔC from 200 kg/m^3 to 800 kg/m^3 reduces τ from 2551 to 637 seconds, but further increasing ΔC to 1600 kg/m^3 reduces τ only to 318 seconds. A similar trend was observed for the changes in μ. Note that in this figure, $\varphi = 0.2$ is assumed.

A parameter sensitivity study was conducted to evaluate the relative influence of v, ΔC, φ, and μ on τ_i predicted by the used the MMDM. The reference parameters ($X_{r(i)}$) were set as $v = 10\ \mu m/s$, $\varphi = 0.1$, $\mu = 1$ Pa·s, and $\Delta C = 1000\ kg/m^3$, yielding a baseline dissolution time of $\tau_r = 790$ seconds. Each parameter (X_i) was varied independently by increasing or decreasing its value fourfold relative to the reference, with a step change of twofold, except ΔC, which was halved. Figure 10 presents the percentage change of τ as a function of parameter variation. For $0.25 \le X_i/X_{r(i)} \le 2$, ΔC has the most significant effect on τ, while μ has the least impact. However, for $2 < X_i/X_{r(i)} \le 4$, φ becomes the most influential parameter, and v has the smallest impact on τ. Consequently, the order of parameter influence is for $0.25 \le X_i/X_{r(i)} \le 2$, $\Delta C > \varphi > v > \mu$, and for $2 < X_i/X_{r(i)} \le 4$, $\varphi > \Delta C > \mu > v$. Moreover, the sensitivity of τ to parameter variations is more pronounced at lower values than at higher ones.

V. CONCLUSION

In this study, two types of porosity level CA2 particles, p-CA2 and d-CA2, were prepared by sintering and arc melting, respectively, with their porosities and surface areas characterized using XCT. The dissolution process of these CA2 particles in CaO-Al_2O_3-SiO_2 type slag was investigated through *in situ* observation. A dissolution model was then developed, incorporating the motion and porosity of CA2 particles. The key findings are as follows:

1. The dissolution behavior of CA2 particles, including motion, dissociation, and interaction with gas bubbles, has been observed and described during the experiments. The first two behaviors enhanced the dissolution of the CA2 particles while the interaction with the gas bubble slowed down dissolution.
2. Increasing the porosity of CA2 particles enhances dissolution kinetics, with the average dissolution rate rising from 0.35 to 0.59 μm/s as porosity increases from 0.08 to 0.20.
3. A mathematical model named "modified mass transfer-controlled dissolution model (MMDM)" was developed by incorporating particle velocity and porosity assuming natural convection. This model can provide a better fit with experimental results as compared to the conventional models lacking these considerations. The MMDM prediction showed that the total dissolution kinetics of CA2 particles was enhanced by an increase in φ, v, and ΔC, and a decrease in μ. The parameter sensitivity analysis found that the order of parameter influence is for $0.25 \le X_i/X_{r(i)} \le 2$, $\Delta C > \varphi > v > \mu$, and for $2 < X_i/X_{r(i)} \le 4$, $\varphi > \Delta C > \mu > v$.

ACKNOWLEDGMENTS

The authors would like to thank the Natural Sciences and Engineering Research Council of Canada (NSERC) for funding this research. This research used a High-Temperature Confocal Laser Scanning Microscopy-VL2000DX-SVF17SP funded by Canada Foundation for Innovation John Evans Leaders Fund (CFI JELF, Project Number: 32826), an X-ray Computed Tomography-Zeiss Xradia 630 Versa located at the Canadian Centre for Electron Microscopy at McMaster University.

CONFLICT OF INTEREST

On behalf of all authors, the corresponding author states that there is no conflict of interest.

NOMENCLATURE

J_1	The mass loss rate of the particle (m/s)
J_2	Mass flux through boundary layer (m/s)
M_P	Mass of particle (kg)
S_S	The nonporous surface area of the particle (μm^2)
S_1	The porous surface area of the particle (μm^2)
ρ_P	Density of particle (kg/m^3)
ρ_S	Density of slag (kg/m3)
r	Radius of particle (μm)
r_0	Initial radius of particle (μm)

τ	Total dissolution time of particle (s)
t	Dissolution time particle (s)
K	Mass transfer coefficient of dissolving species (m/s)
D	Diffusion coefficient of dissolving species (m^2/s)
C_{sat}	Saturation concentration of dissolving species (kg/m^3)
C_0	Concentration of dissolving species in bulk slag (kg/m^3)
C_P	The concentration of dissolving species in particles (kg/m^3)
ΔC	Concentration of dissolving species between that at x and bulk slag (kg/m^3)
φ	Porosity of particle
Pe	Péclet number
Re	Reynolds number
v	Velocity of particle (m/s)
μ_S	Viscosity of slag (Pa·s)
C_D	Drag coefficient
g	Gravity (m/s^2)

REFERENCES

1. C.J. Xuan and W.Z. Mu: *J. Am. Ceram. Soc.*, 2020, vol. 104, pp. 57–75.
2. R. Li, X. Wang, X. Gao, W. Wang, and Y. Zhou: *Ceram. Int.*, 2024, vol. 50, pp. 8249–59.
3. A.J. Deng, H.C. Wang, and D.D. Fan: *ISIJ Int.*, 2021, vol. 61, pp. 2475–82.
4. M. Sharma, W. Mu, and N. Dogan: *JOM*, 2018, vol. 70, pp. 1220–24.
5. C.J. Xuan and W.Z. Mu: *J. Am. Ceram. Soc.*, 2019, vol. 102, pp. 6480–97.
6. J.J. Liu, J. Zou, M.X. Guo, and N. Moelans: *Comput. Mater. Sci.*, 2016, vol. 119, pp. 9–18.
7. J. Heulens, B. Blanpain, and N. Moelans: *Acta Mater.*, 2011, vol. 59, pp. 2156–65.
8. F. Verhaeghe, S. Arnout, B. Blanpain, and P. Wollants: *Phys. Rev. E*, 2006, vol. 73, p. 036316.
9. S. Sridhar and A.W. Cramb: *Metall. Mater. Trans. B*, 2000, vol. 31B, pp. 406–10.
10. S. Feichtinger, S.K. Michelic, Y.B. Kang, and C. Bernhard: *J. Am. Ceram. Soc.*, 2014, vol. 97, pp. 316–25.
11. K.Y. Miao, A. Haas, M. Sharma, W.Z. Mu, and N. Dogan: *Metall. Mater. Trans. B*, 2018, vol. 49B, pp. 1612–23.
12. J.H. Park, I.H. Jung, and H.G. Lee: *ISIJ Int.*, 2006, vol. 46, pp. 1626–34.
13. X.L. Guo, J.V. Dyck, M.X. Guo, and B. Blanpain: *AIChE J.*, 2013, vol. 59, pp. 2907–16.
14. Z. Deng, X. Zhang, G. Hao, C. Wei, and M. Zhu: *Int. J. Miner. Metall. Mater.*, 2024, vol. 31, pp. 977–87.
15. L.J. Zhou, W.L. Wang, F.J. Ma, J. Li, J. Wei, H. Matsuura, and F. Tsukihashi: *Metall. Mater. Trans. B*, 2011, vol. 43B, pp. 354–62.
16. Y. Kim, Y. Kashiwaya, and Y. Chung: *Ceram. Int.*, 2020, vol. 46, pp. 6205–11.
17. Y.Z. Huo, H.Z. Gu, A. Huang, B.Y. Ma, L.Y. Chen, G.Q. Li, and Y.W. Li: *J. Iron. Steel Res. Int.*, 2022, vol. 29, pp. 1711–22.
18. C. Tse, S.H. Lee, K.W. Yi, P. Misra, V. Chevrier, and C. Orrling: *J. Non-Cryst. Solids*, 2001, vol. 282, pp. 41–48.
19. G. Wang, M. Nabeel, W.Z. Mu, A.B. Phillion, and N. Dogan: *J. Iron. Steel Res. Int.*, 2025, vol. 32, pp. 364–75.
20. G. Kim and Y. Chung: *Steel Res. Int.*, 2024, https://doi.org/10.1002/srin.202400039.
21. Y. Ren, P. Zhu, C. Ren, N. Liu, and L. Zhang: *Metall. Mater. Trans. B*, 2022, vol. 53B, pp. 682–92.
22. M. Valdez, K. Prapakorn, A.W. Cramb, and S. Sridhar: *Steel Res. Int.*, 2001, vol. 72, pp. 291–97.
23. M. Valdez, K. Prapakorn, A.W. Cramb, and S. Sridhar: *Ironmak. Steelmak.*, 2002, vol. 29, pp. 47–52.
24. K.W. Yi, C. Tse, J.H. Park, M. Valdez, A.W. Cramb, and S. Sridhar: *Scand. J. Metall.*, 2003, vol. 32, pp. 177–84.
25. A.B. Fox, J. Gisby, R.C. Atwood, P.D. Lee, and S. Sridhar: *ISIJ Int.*, 2004, vol. 44, pp. 836–45.
26. L. Chen and B.J. Monaghan: *J. Non-Cryst. Solids*, 2004, vol. 347, pp. 254–61.
27. B.J. Monaghan, L. Chen, and J. Sorbe: *Ironmak. Steelmak.*, 2005, vol. 32, pp. 258–64.
28. B.J. Monaghan and L. Chen: *Steel Res. Int.*, 2005, vol. 76, pp. 348–54.
29. J. Liu, M. Guo, P.T. Jones, F. Verhaeghe, B. Blanpain, and P. Wollants: *J. Am. Ceram. Soc.*, 2007, vol. 90, pp. 3818–24.
30. F. Verhaeghe, J. Liu, M. Guo, S. Arnout, B. Blanpain, and P. Wollants: *Appl. Phys. Lett.*, 2007, vol. 91, p. 124104.
31. F. Verhaeghe, J. Liu, M. Guo, S. Arnout, B. Blanpain, and P. Wollants: *J. Appl. Phys.*, 2008, vol. 103, p. 023506.
32. S. Michelic, J. Goriupp, S. Feichtinger, Y.B. Kang, C. Bernhard, and J. Schenk: *Steel Res. Int.*, 2016, vol. 87, pp. 57–67.
33. C. Ren, L. Zhang, J. Zhang, S. Wu, P. Zhu, and Y. Ren: *Metall. Mater. Trans. B*, 2021, vol. 52, pp. 3288–3301.
34. C. Ren, C. Huang, L. Zhang, and Y. Ren: *Int. J. Miner. Metall. Mater.*, 2023, vol. 30, pp. 345–53.
35. J. Liu, M. Guo, P.T. Jones, F. Verhaeghe, B. Blanpain, and P. Wollants: *J. Eur. Ceram. Soc.*, 2007, vol. 27, pp. 1961–72.
36. X.L. Guo, Z.H.I. Sun, J.V. Dyck, M.X. Guo, and B. Blanpain: *Ind. Eng. Chem. Res.*, 2014, vol. 53, pp. 6325–33.
37. T. Tian, Y. Zhang, H. Zhang, K. Zhang, J. Li, and H. Wang: *Int. J. Appl. Ceram. Technol.*, 2019, vol. 16, pp. 1078–87.
38. B.J. Monaghan and L. Chen: *Ironmak. Steelmak.*, 2006, vol. 33, pp. 323–30.
39. M. Sharma and N. Dogan: *Metall. Mater. Trans. B*, 2020, vol. 51B, pp. 570–80.
40. O. Levenspiel: *Chemical Reaction Engineering*, Wiley, New York, 1998.
41. M.J. Whelan: *Met. Sci. J.*, 1969, vol. 3, pp. 95–97.
42. P. Yan, B.A. Webler, P.C. Pistorius, and R.J. Fruehan: *Metall. Mater. Trans. B*, 2015, vol. 46B, pp. 2414–18.
43. L.C. Zheng, A. Malfliet, B.Q. Yan, Z.H. Jiang, B. Blanpain, and M.X. Guo: *ISIJ Int.*, 2022, vol. 62, pp. 1573–85.
44. S.K. Michelic and C. Bernhard: *Steel Res. Int.*, 2022, vol. 93, p. 2200086.
45. H.B. Yin, H. Shibata, T. EmIand, and M. Suzuk: *ISIJ Int.*, 1997, vol. 37, p. 10.
46. H. Chikama, H. Shibata, T. EmIand, and M. Suzuk: *Mater. Trans. JIM*, 1996, vol. 37, pp. 620–26.
47. C. Orrling, Y. Fang, N. Phinichka, S. Sridhar, and A.W. Cramb: *JOM-e* 1999, vol. 51.
48. C.A. Schneider, W.S. Rasband, and K.W. Eliceiri: *Nat. Methods*, 2012, vol. 9, pp. 671–75.
49. T.K. Sherwood, R.L. Pigford, and C.R. Wilke: *Mass Transfer*, McGraw-Hill, New York, 1975.
50. Y.X. Zhang and Z.J. Xu: *Earth Planet. Sci. Lett.*, 2003, vol. 213, pp. 133–48.
51. D.L. Turcotte and G. Schubert: *Geodynamics Applications of Continuum Physics to Geological Problems*, Wiley, New York, 1982.
52. V.I. Ponomarev, D.M. Kheiker, and N.V. Belov: *Sovit Phys. Crystallogr.*, 1971, vol. 15, pp. 995–1002.
53. C.W. Bale, E. Bélisle, P. Chartrand, S.A. Decterov, G. Eriksson, A.E. Gheribi, K. Hack, I.H. Jung, Y.B. Kang, J. Melançon, A.D. Pelton, S. Petersen, C. Robelin, J. Sangster, P. Spencer, and M.A. Ende: *Calphad*, 2016, vol. 55, pp. 1–19.